ARCHIVE OF MECHANICAL ENGINEERING

DOI: 10.24425/ame.2022.144075 2023, Vol. 70, No. 1, pp. 151–178

Robert GŁĘBOCKI [1], Marcin ŻUGAJ [1], Mariusz JACEWICZ [1]

Validation of the energy consumption model for a quadrotor using Monte-Carlo simulation

Received 21 May 2022, **Revised** 17 November 2022, **Accepted** 30 November 2022, **Published online** 8 December 2022

Keywords: quadrotor, flight tests, energy consumption, battery

Unmanned, battery-powered quadrotors have a limited onboard energy resources. However, flight duration might be increased by reasonable energy expenditure. A reliable mathematical model of the drone is required to plan the optimum energy management during the mission. In this paper, the theoretical energy consumption model was proposed. A small, low-cost DJI MAVIC 2 Pro quadrotor was used as a test platform. Model parameters were obtained experimentally in laboratory conditions. Next, the model was implemented in MATLAB/Simulink and then validated using the data collected during real flight trials in outdoor conditions. Finally, the Monte-Carlo simulation was used to evaluate the model reliability in the presence of modeling uncertainties. It was obtained that the parameter uncertainties could affect the amount of total consumed energy by less than 8% of the nominal value. The presented model of energy consumption might be practically used to predict energy expenditure, battery state of charge, and voltage in a typical mission of a drone.

1. Introduction

In recent years, quadrotors have become very popular and are now used in a wide area of applications, e.g., agriculture, aerial imaging, search & rescue missions, package delivery, reconnaissance, inspection, etc. [1, 2]. Vertical take-off and landing capability, high maneuverability, relatively simple mechanical design, and low cost give them advantages over fixed-wing drones and helicopters. They are often powered by Lithium-Ion multiple-use batteries. These batteries offer a high energy density, lack of memory effects, and low mass.

✉ Mariusz Jacewicz, e-mail: mariusz.jacewicz@pw.edu.pl

[1] Warsaw University of Technology, Faculty of Power and Aeronautical Engineering, Warsaw, Poland. ORCIDs: R.G. 0000-0002-2389-7653; M.Ż. 0000-0003-0944-4516; M.J. 0000-0002-7173-0890

One of the main problems with quadrotors is limited energy available onboard and quite a large energy consumption, resulting in a short time of flight duration and a short range. A large amount of energy is spent on propulsion to maintain the drone in the air. The quantity of the consumed energy might depend on several factors (e.g., flight velocity, motor angular rates, environmental conditions, time of flight, and altitude) [3, 4]. The mission should be planned carefully to maximize flight efficiency. To realize this goal, a reliable mathematical model of the energy consumption by the drone in various flight conditions is necessary.

The topic of electrical energy consumption by quadrotors was previously studied by several researchers, and some energetic models were proposed. Those models might be divided into three main groups: based on the physical properties of the quadrotor system, experimental data fitting, and aeromechanics theories.

The first group of models relies on a detailed model of the quadrotor itself and the propulsion system [5–8]. The main advantage of such a methodology is that they allow for deep insight into the system dynamics [9]. However, such models also require a set of parameters [10, 11] that must be estimated carefully to make the simulation reliable and realistic. Very often, only the energy consumed by the main rotors is considered [12, 13]. Neglecting energy consumption by onboard subsystems, this approach might lead to overestimating the real flight duration. In the existing models, sometimes it is assumed that the quadrotor is in a steady state flight [14] which is not always a valid assumption. Moreover, some of the presented quadrotor energy consumption models are investigated using only simulation but not validated using real data. Very simplified models of energy consumption [15–18] might also be included in this category.

The second approach is based on the black-box models [19–21]. Up to this time, several empirical models were also proposed [22, 23]. Such models are based on polynomial fitting functions with arguments like altitude, velocity, and payload. These models do not require physical parameters, and this is a significant advantage over model-based approaches. The total consumed energy is calculated as a sum of energies required in various flight phases, including hovering, accelerating, decelerating, and turning [24]. The main disadvantage of this method is that this approach of modeling does not allow for deep insight into quadcopter flight parameters. The consumed energy is modeled as a function of speed and acceleration [25, 26] using curve fitting techniques.

The third group of models uses aeromechanics to predict the consumed energy [27]. The Momentum Theory was used extensively to predict the energy consumption in hover and forward flight [28–31]. More advanced approaches use Blade Element Theory to predict energy consumption [32]. The advantage of these models is a detailed insight into rotor dynamics and flow phenomena. However, for practical purposes, such models are often simplified and do not take into account some physical phenomena [33]. The main drawback of such models is that they are complicated and require several parameters that might be difficult to obtain. Also, the induced velocity must be calculated by solving the nonlinear equation itera-

tively, which slows down the simulation speed when compared to other modeling approaches.

The battery dynamic is often not included in the existing models. This leads to large uncertainties in predicted flight endurance [34]. The battery voltage decreases slowly during the flight, and as a result, the available power at the beginning of the flight is smaller than at the end of the flight. Moreover, the existing models have not been validated carefully. The described experiments are often limited to laboratory trials or short-duration flights in indoor conditions.

The goal of the study presented here was to develop and validate a reliable simulation model of energy consumption by a quadrotor in a typical mission. Such a model might be practically used for mission planning and trajectory optimization purposes.

The main challenge was that the DJI Mavic 2 Pro drone (that was used in the research) was very difficult to modify. Adding some external measurement instrumentation results in the degradation of drone performance. Due to this reason, only built-in functionalities were used to obtain the flight data. The test platform has a closed architecture with a minimum possibility of configuration. That fact makes the modeling process much harder. Such a situation is quite often present in the case of commercial drones.

The main contribution of this paper is the comparison of the calculated results with the data from the real flight tests of energy consumption realized in a windy environment. The model parameters were evaluated experimentally.

The structure of the paper is as follows. In Section 2 the test platform and nonlinear mathematical model of the object are presented. The assumed autopilot structure and energy consumption model are also described. In Section 3 flight tests are explained, and model validation is shown. This manuscript ends with a discussion of the obtained results and a summary of the main findings. Further research directions are also considered.

2. Materials and methods

2.1. Test platform

The commercially available DJI MAVIC 2 Pro quadcopter was used as a test mobile platform [35]. The drone operated in the cross-configuration and was modified to integrate an object with pads of a ground charging station (e.g., legs were added). The total mass of the drone (after modifications) is $m = 0.960$ kg and the mass without propellers and legs is 0.873 kg. Moments of inertia with respect to the center of mass are (configuration without propellers): $I_{xx} = 4.25582 \cdot 10^{-3}$ kgm^2, $I_{yy} = 4.724053 \cdot 10^{-3}$ kgm^2, $I_{zz} = 7.859282 \cdot 10^{-3}$ kgm^2. The moments of inertia were estimated experimentally using a trifilar pendulum (Fig.1) and confirmed using a CAD model. The products of inertia $I_{xy} = I_{yz} = 0$ (due to symmetry) and I_{xz} were assumed to be negligible.

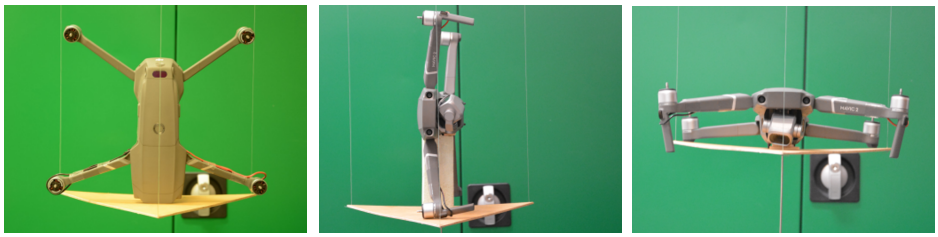

(a) longitudinal axis (b) lateral axis (c) vertical axis

Fig. 1. Moments of inertia measurements using a trifilar pendulum

The parameters of propellers were obtained from experimental measurements. The mass of the single, fixed-pitch propeller is 0.0079 kg. The moment of inertia of the rotating parts (one propeller + shaft) with respect to the rotation axis is $I_{zzp} = 3.2127 \cdot 10^{-5}$ kgm^2. The propeller diameter is $D_p = 0.22$ m and thread pitch 0.1092 m. Propellers number 1 (forward right) and 3 (aft left) rotate counterclockwise, looking from the top, whereas 2 (aft right) and 4 (forward left) spin clockwise. The propeller chord distribution c is presented in Fig. 2 as a function of radial distance ($r = 0$ mm – blade root, $r = 110$ mm – blade tip).

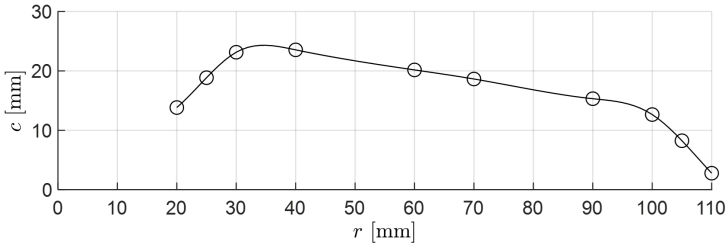

Fig. 2. Propeller geometry

The drone is equipped with a vision system (a gimbaled camera + side cameras) and several onboard sensors (accelerometers, gyroscopes, magnetometer, sonar, and barometer). A set of flight data parameters could be recorded during the mission using the built-in functionality.

2.2. Model assumptions

It was assumed that the quadrotor is a rigid body with 6 degrees of freedom (DOF) and a constant mass. The aerodynamic interference between rotors and fuselage, as well as the ground effect, were neglected. It was also assumed that all four motors were identical. The motor dynamic was included in the model. The Earth rotation effects were omitted. Gravity acceleration g was calculated using the WGS-84 model. Air properties were obtained according to the ISA Atmosphere model [36]. The wind field was incorporated into the simulation. The quadrotor model includes battery dynamics.

2.3. Coordinate frames

In Fig. 3 the coordinate systems used in the mathematical model are shown.

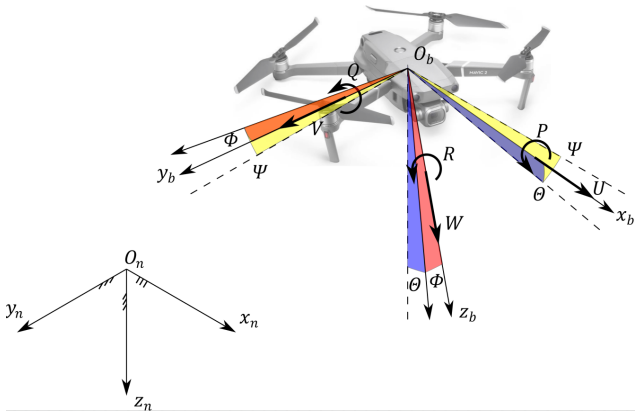

Fig. 3. Coordinate systems used in the model

$O_n x_n y_n z_n$ is the Earth-fixed North-East-Down oriented coordinate frame. On the other hand, $O_b x_b y_b z_b$ frame is rigidly attached to the quadrotor and moves with the object. Origin O_b is located at the center of mass of the drone, $O_b x_b$ axis is pointed forward, $O_b y_b$ to the right and $O_b z_b$ is pointed down. The state vector of the system is $\boldsymbol{x}_{\text{state}} = \begin{bmatrix} U & V & W & P & Q & R & x_n & y_n & z_n & e_0 & e_1 & e_2 & e_3 \end{bmatrix}^T$ where: U, V, W – linear quasi-velocities in $O_b x_b y_b z_b$ frame, P, Q, R – quasi-angular rates in $O_b x_b y_b z_b$ frame, x_n, y_n, z_n – drone center of mass position coordinates in $O_n x_n y_n z_n$ frame, $e_0 e_1 e_2 e_3$ – quaternion elements. The z_n is the vertical coordinate that relates to the altitude h by equation $h = -z_n$.

Quaternions were used to describe the object's attitude. The method of algebraic constraint [37, 38] was applied to improve the accuracy of the numerical calculations:

$$\begin{bmatrix} \dot{e}_0 \\ \dot{e}_1 \\ \dot{e}_2 \\ \dot{e}_3 \end{bmatrix} = -\frac{1}{2} \begin{bmatrix} 0 & P & Q & R \\ -P & 0 & -R & Q \\ -Q & R & 0 & -P \\ -R & -Q & P & 0 \end{bmatrix} \begin{bmatrix} e_0 \\ e_1 \\ e_2 \\ e_3 \end{bmatrix} - kE \begin{bmatrix} e_0 \\ e_1 \\ e_2 \\ e_3 \end{bmatrix}, \tag{1}$$

where: k – constant coefficient, E – constraint ($E = 0$ in an ideal situation), which is given as [37] $E = e_0^2 + e_1^2 + e_2^2 + e_3^2 - 1$. The coefficient k is often chosen empirically to ensure $k h_{\text{int}} \leqslant 1$, where h_{int} is a numerical integration step [38] (it was assumed that $k = 1$). The integration in time of (1) allows obtaining quaternion e_0, e_1, e_2, e_3 that describes the attitude.

The kinematic relations between the position coordinates in $O_n x_n y_n z_n$ frame and quasi-velocities in $O_b x_b y_b z_b$ are [37–39]:

$$\begin{bmatrix} \dot{x}_n \\ \dot{y}_n \\ \dot{z}_n \end{bmatrix} = \begin{bmatrix} e_0^2 + e_1^2 - e_2^2 - e_3^2 & 2(e_1 e_2 - e_0 e_3) & 2(e_0 e_2 + e_1 e_3) \\ 2(e_0 e_3 + e_1 e_2) & e_0^2 - e_1^2 + e_2^2 - e_3^2 & 2(e_2 e_3 - e_0 e_1) \\ 2(e_1 e_3 - e_0 e_2) & 2(e_0 e_1 + e_2 e_3) & e_0^2 - e_1^2 - e_2^2 + e_3^2 \end{bmatrix} \begin{bmatrix} U \\ V \\ W \end{bmatrix}. \tag{2}$$

For post-processing purposes, the Euler angles were calculated as [37, 40]:

$$\Phi = \arctan\left[\frac{2(e_0 e_1 + e_2 e_3)}{e_0^2 - e_1^2 - e_2^2 + e_3^2}\right], \tag{3}$$

$$\Theta = \arcsin\left[2(e_0 e_2 - e_1 e_3)\right], \tag{4}$$

$$\Psi = \arctan\left[\frac{2(e_0 e_3 + e_1 e_2)}{e_0^2 + e_1^2 - e_2^2 - e_3^2}\right]. \tag{5}$$

To integrate (1), it is necessary to calculate the initial quaternion values. The initial altitude was defined by Euler angles Φ, Θ, Ψ, and then recalculated on quaternions (details could be found in [37, 40]).

2.4. Dynamic equations of motion

The dynamic equations of motion were obtained using momentum $\boldsymbol{\Pi}$ and angular momentum $\boldsymbol{K}_0$ change theorems, which in a non-inertial frame $O_b x_b y_b z_b$ have the form [41]:

$$\frac{\tilde{\delta}\boldsymbol{\Pi}}{\tilde{\delta}t} + \boldsymbol{\Omega} \times \boldsymbol{\Pi} = \boldsymbol{F}_b, \tag{6}$$

$$\frac{\tilde{\delta}\boldsymbol{K}_0}{\tilde{\delta}t} + \boldsymbol{\Omega} \times \boldsymbol{K}_0 = \boldsymbol{M}_b, \tag{7}$$

where $\boldsymbol{\Omega} = \begin{bmatrix} P & Q & R \end{bmatrix}^T$ vector of quasi-angular rates, $\boldsymbol{F}_b = \begin{bmatrix} X_b & Y_b & Z_b \end{bmatrix}^T$ vector of external forces expressed in $O_b x_b y_b z_b$, $\boldsymbol{M}_b = \begin{bmatrix} L_b & M_b & N_b \end{bmatrix}^T$ vector of external moments with respect to the point O_b, and $\frac{\tilde{\delta}}{\tilde{\delta}t}$ is a local derivative. If O_b coincides with the center of mass of the quadrotor, momentum $\boldsymbol{\Pi}$ is given as:

$$\boldsymbol{\Pi} = m\boldsymbol{V}_b, \tag{8}$$

where m – quadrotor mass, $\boldsymbol{V}_b = \begin{bmatrix} U & V & W \end{bmatrix}^T$ – vector of quasi-velocities in $O_b x_b y_b z_b$ frame. The angular momentum with respect to the origin of $O_b x_b y_b z_b$ frame is given as:

$$\boldsymbol{K}_0 = \boldsymbol{I}\,\boldsymbol{\Omega}, \tag{9}$$

where $\boldsymbol{I}$ is the inertia matrix defined as [39] $\boldsymbol{I} = \text{diag}(I_{xx}, I_{yy}, I_{zz})$ and I_{xx}, I_{yy}, I_{zz} are moments of inertia in $O_b x_b y_b z_b$ frame. When (8) and (9) are substituted into (6) and (7) (ignoring products of inertia), the equations of motion are [41]:

$$m\left(\dot{U} + WQ - VR\right) = X_b\,, \tag{10}$$

$$m\left(\dot{V} + UR - WP\right) = Y_b\,, \tag{11}$$

$$m\left(\dot{W} + VP - UQ\right) = Z_b\,, \tag{12}$$

$$I_{xx}\dot{P} - \left(I_{yy} - I_{zz}\right)RQ = L_b\,, \tag{13}$$

$$I_{yy}\dot{Q} - \left(I_{zz} - I_{xx}\right)PR = M_b\,, \tag{14}$$

$$I_{zz}\dot{R} - \left(I_{xx} - I_{yy}\right)PQ = N_b\,. \tag{15}$$

2.5. External forces and moments

The total external forces $\boldsymbol{F}_b$ acting on the quadrotor expressed in $O_b x_b y_b z_b$ frame are:

$$\boldsymbol{F}_b = \begin{bmatrix} X_b, & Y_b, & Z_b \end{bmatrix}^T = \boldsymbol{F}_g + \boldsymbol{F}_p + \boldsymbol{F}_a\,, \tag{16}$$

where: $\boldsymbol{F}_g$ – gravity forces, $\boldsymbol{F}_p$ – forces from propellers, $\boldsymbol{F}_a$ – fuselage aerodynamic loads.

The moments $\boldsymbol{M}_b$ expressed in $O_b x_b y_b z_b$ with respect to the origin O_b are:

$$\boldsymbol{M}_b = \begin{bmatrix} L_b, & M_b, & N_b \end{bmatrix}^T = \boldsymbol{M}_g + \boldsymbol{M}_p + \boldsymbol{M}_a\,, \tag{17}$$

where: $\boldsymbol{M}_g$ – moments from gravity, $\boldsymbol{M}_p$ – moments from the propellers and $\boldsymbol{M}_a$ – aerodynamics moments.

2.5.1. Gravity loads

Gravity forces $\boldsymbol{F}_g$ expressed in $O_b x_b y_b z_b$ are [42, 43]:

$$\boldsymbol{F}_g = \begin{bmatrix} X_g, & Y_g, & Z_g \end{bmatrix}^T = mg \begin{bmatrix} -\sin\Theta, & \cos\Theta\sin\Phi, & \cos\Theta\cos\Phi \end{bmatrix}^T. \tag{18}$$

It was assumed that the origin O_b coincides with the center of mass of the object, so moments $\boldsymbol{M}_g$ are equal zero.

2.5.2. Loads generated by propellers

Total forces generated by four propellers are calculated as a sum of forces from individual propellers:

$$\boldsymbol{F}_p = \begin{bmatrix} X_p, & Y_p, & Z_p \end{bmatrix}^T = \sum_{j=1}^{4} \boldsymbol{F}_{pj}\,, \tag{19}$$

where $j = \{1 \ldots 4\}$ is the number of the j-th propeller. The force generated by a single propeller in $O_b x_b y_b z_b$ is [44]:

$$\boldsymbol{F}_{pj} = \begin{bmatrix} X_{pj}, & Y_{pj}, & Z_{pj} \end{bmatrix}^T = \begin{bmatrix} 0, & 0, & -T_j \end{bmatrix}^T . \tag{20}$$

The thrust force T_j generated by the j-th propeller is proportional to the angular rate Ω_j [45–48]:

$$T_j = \rho S_p R_p^2 \Omega_j^2 k_f \,, \tag{21}$$

where: ρ – air density, $S_p = \pi R_p^2$ – area of propeller disc, R_p – propeller radius, k_f – thrust coefficient ($k_f = 1.353 \cdot 10^{-4}$ N/RPM^2).

Moments generated by a single the j-th propeller with respect to point O_b expressed in $O_b x_b y_b z_b$ are:

$$\boldsymbol{M}_{pj} = \begin{bmatrix} L_{pj}, & M_{pj}, & N_{pj} \end{bmatrix}^T = \boldsymbol{r}_{pj} \times \boldsymbol{F}_{pj} + \begin{bmatrix} 0 \\ 0 \\ -M_j \end{bmatrix} (-1)^j, \tag{22}$$

where $\boldsymbol{r}_{pj} = \begin{bmatrix} r_{pjx} & r_{pjy} & r_{pjz} \end{bmatrix}^T$ is a vector with the origin in point O_b and the end in the point of mounting the propeller. The vectors $\boldsymbol{r}_{pj}$ for each of the propellers are: $\boldsymbol{r}_{p1} = \begin{bmatrix} 0.108, & 0.139, & 0 \end{bmatrix}^T$ m, $\boldsymbol{r}_{p2} = \begin{bmatrix} -0.108, & 0.139, & 0 \end{bmatrix}^T$ m, $\boldsymbol{r}_{p3} = \begin{bmatrix} -0.108, & -0.139, & 0 \end{bmatrix}^T$ m and $\boldsymbol{r}_{p4} = \begin{bmatrix} 0.108, & -0.139, & 0 \end{bmatrix}^T$ m. Drag moment M_j of the j-th propeller is calculated as [45]:

$$M_j = \rho S_p R_p^3 \Omega_j^2 k_m \,, \tag{23}$$

where k_m propeller drag coefficient ($k_m = 2.8 \cdot 10^{-5}$ Nm/RPM^2). Coefficients k_f and k_m have been found experimentally and compared with the data available in the literature. The gyroscopic effects caused by propellers rotations were omitted in the presented model.

2.5.3. Aerodynamic loads generated by the airframe

In the aerodynamic model of the fuselage, only a drag force was considered. Aerodynamic forces generated by the fuselage and expressed in $O_b x_b y_b z_b$ frame are defined as:

$$\boldsymbol{F}_a = \begin{bmatrix} X_a, & Y_a, & Z_a \end{bmatrix}^T = \frac{1}{2} \rho V_{\text{tot}}^2 S \begin{bmatrix} C_X \cos\alpha \cos\beta \\ C_X \sin\beta \\ C_X \sin\alpha \cos\beta \end{bmatrix}, \tag{24}$$

where: ρ – air density, V_{tot} – total flight velocity, S – reference area (assumed 1 m^2), C_X – drag force coefficient, α – the angle of attack, β – the angle of sideslip.

Aerodynamic moments $\boldsymbol{M}_a$ with respect to the point O_b expressed in $O_b x_b y_b z_b$ are equal zero.

It was assumed that the aerodynamic drag coefficient is a function of angles of attack and sideslip. The angle of attack α is defined as [37]:

$$\alpha = \arctan \frac{W - W_W}{U - U_W} \,. \tag{25}$$

In the numerical simulation, the function $\arctan 2(W - W_W,\, U - U_W)$ was used to ensure the values of α from –180° up to 180°. The angle of sideslip β is [37]:

$$\beta = \arcsin \frac{V - V_W}{V_{\text{tot}}} \,. \tag{26}$$

The total flight velocity with respect to the oncoming flow V_{tot} is calculated as:

$$V_{\text{tot}} = \sqrt{(U - U_W)^2 + (V - V_W)^2 + (W - W_W)^2} \,, \tag{27}$$

where U_w, V_W, W_W are linear wind velocities in the body-fixed frame $O_b x_b y_b z_b$. The drag coefficient was estimated from the flight data. The lookup table methodology was used to implement the fuselage aerodynamic drag coefficient as a function of two inflow angles.

2.6. Electric motor model

It was assumed that all four brushless direct-current (BLDC) motors are the same. The shaft is connected to the propeller hub directly (without a gearbox). Each of the motors was modeled using the first-order transfer function:

$$\Omega_j = \frac{1}{T_s s + 1} \Omega_{jc} \,, \tag{28}$$

where: Ω_{jc} – commanded angular rate (obtained from (43)), T_s – time constant (it was assumed 0.05 s). The upper saturation of angular speed was included in the model. It was found experimentally that the maximum achievable propeller angular speed for the tested drone is 9800 RPM. Under these conditions, the tip speed of the propeller is 112.89 m/s. The angular rate of the propellers at hover is approximately 5300 RPM.

2.7. Wind model

The wind is an important factor that affects the amount of energy consumed. Due to this reason, the wind effects were included in the model. A uniform wind

field was considered. The total wind velocity expressed in $O_n x_n y_n z_n$ coordinate frame is $V_{W\,tot}$, and the direction of the oncoming wind is defined by the angle Ψ_W (clockwise when looking from the top, e.g., 0° means wind from the North, 90° from the East). The wind velocities in $O_n x_n y_n z_n$ frame are:

$$\begin{bmatrix} U_{Wn} \\ V_{Wn} \\ W_{Wn} \end{bmatrix} = \begin{bmatrix} -V_{W\,\mathrm{tot}} \cos \Psi_W \\ -V_{W\,\mathrm{tot}} \sin \Psi_W \\ 0 \end{bmatrix}. \tag{29}$$

Next, the wind velocities U_{Wn}, V_{Wn}, W_{Wn} are transformed from $O_n x_n y_n z_n$ to body-fixed frame $O_b x_b y_b z_b$:

$$\begin{bmatrix} U_W \\ V_W \\ W_W \end{bmatrix} = \begin{bmatrix} \cos\theta\cos\Psi & \cos\theta\cos\Psi & -\sin\theta \\ \sin\Phi\sin\theta\cos\Psi - \cos\Phi\sin\Psi & \sin\Phi\sin\theta\sin\Psi + \cos\Phi\cos\Psi & \sin\Phi\cos\theta \\ \cos\Phi\sin\theta\cos\Psi - \cos\Phi\sin\Psi & \cos\Phi\sin\theta\sin\Psi - \sin\Phi\cos\Psi & \cos\Phi\cos\theta \end{bmatrix} \times \begin{bmatrix} U_{Wn} \\ V_{Wn} \\ W_{Wn} \end{bmatrix}. \tag{30}$$

During the experiments, the wind speed $V_{W\,\mathrm{tot}}$ and azimuth Ψ_W have been measured during the flight on the ground using a digital anemometer. Additionally, these parameters might be estimated after the flight from data logs using the Airdata online tool [49]. The calculated wind velocities are input data for equations (25), (26), and (27).

2.8. Energy consumption model

The 6 DOF model was used to calculate the flight parameters (among others, motors' angular rates) that can be used in order to predict energy consumption. The test platform is equipped with a single Lithium-Polymer, rechargeable, four-cell battery. This kind of battery offers a high energy density, a high rate of charge/discharge, and a relatively low cost [6]. For the fully charged battery, the flight endurance is approximately 31 min. The onboard battery parameters declared by the Manufacturer are as follows [35]: capacity 3850 mAh, voltage 15.4 V, maximum charging voltage 17.6 V, stored energy 59.29 Wh and mass 297 g.

The total energy consumption E_c is a sum of two components: energy consumed by all four electric motors E_m and energy used by onboard systems other

than motors (e.g., sensors, remote control receiver, autopilot, LED indicators, and other circuits) E_s [5, 50]:

$$E_c = E_m + E_s \,. \tag{31}$$

Energy used for propulsion E_m is often considerably higher than for powering the onboard systems E_s [26].

Energy consumed by all four motors could be calculated as [7, 10, 51, 52]:

$$E_m = \int_{t_0}^{t_k} \sum_{j=1}^{4} U_j(t) I_j(t) \, \mathrm{d}t, \tag{32}$$

where: $U_j(t)$ – voltage of the j-th motor, $I_j(t)$ – electric current on the j-th motor, t_0 – initial time (in most cases 0 [s]), t_k – total quadrotor flight time, $j = \{1, 2, 3, 4\}$ – motor number. The current was not measured directly by the onboard equipment, so it was necessary to write (32) in terms of motor speed instead of current. The speed of each motor is obtained from the previously described 6 DOF quadrotor model. Energy E_m consumed by all the electric motors could be written as [8]:

$$E_m = \int_{t_0}^{t_k} \sum_{j=1}^{4} \tau_j(t) \Omega_j(t) \, \mathrm{d}t, \tag{33}$$

where: $\tau_j(t)$ – torque generated by the j-th motor, $\Omega_j(t)$ – angular speed of the j-th motor, $j = t\{1, 2, 3, 4\}$ – motor number. The dynamic of the motor might be expressed as [7]:

$$I_{zzp} \dot{\Omega}_j(t) = \tau_j(t) - k_m \Omega_j^2(t) + D_v \Omega_j(t), \tag{34}$$

where: I_{zzp} – moment of inertia of rotating parts (propeller and rotor shaft, together) with respect to its rotation axis, k_m – drag coefficient of the propeller, D_v – viscous damping coefficient of the motor (assumed $1 \cdot 10^{-4}$ Nm·s/rad). The dot symbol above some quantities denotes the first derivative with respect to time. Using (34) the equation (33) could be transformed to [8]:

$$E_m = \int_{t_0}^{t_k} \sum_{j=1}^{4} \left(I_{zzp} \dot{\Omega}_j(t) + k_m \Omega_j^2(t) + D_v \Omega_j(t) \right) \Omega_j(t) \, \mathrm{d}t. \tag{35}$$

A motor efficiency was included in the equations to increase model fidelity [8]:

$$E_m = \int_{t_0}^{t_k} \sum_{j=1}^{4} \frac{I_{zzp} \dot{\Omega}_j(t) + k \Omega_j^2(t) + D_v \Omega_j(t)}{f_{r,j}\left(\tau_j(t), \Omega_j(t)\right)} \Omega_j(t) \, \mathrm{d}t, \tag{36}$$

where: $f_{r,j}\left(\tau_j(t), \Omega_j(t)\right)$ – efficiency of the j-th electric motor that depends on the torque and angular speed of the motor. Some data about motor efficiency were delivered by the producer. MATLAB Curve Fitting toolbox was used to find the polynomial that represents the existing data (R-square = 0.9997):

$$f_{r,j}\left(\Omega_j(t)\right) = a_5\Omega_j^5(t) + a_4\Omega_j^4(t) + a_3\Omega_j^3(t) + a_2\Omega_j^2(t) + a_1\Omega_j(t) + a_0\,, \quad (37)$$

where: $a_5 = -6.106\text{e}{-20}$, $a_4 = 1.603\text{e}{-15}$, $a_3 = -1.309\text{e}{-11}$, $a_2 = 1.23\text{e}{-08}$, $a_1 = 0.0002893$, $a_0 = -0.006304$ and $\Omega_j(t) \in \langle 0;\ 900\rangle$ RPM.

The total energy consumed by the onboard subsystems was calculated as:

$$E_s = \int_{t_0}^{t_k} E_{\text{sub}}\,\mathrm{d}t, \quad (38)$$

where E_{sub} – instantaneous power consumption. The value of E_{sub} was obtained experimentally by on-ground, stationary tests in laboratory conditions. The experimental setup (Fig. 4) was composed of a charger/discharger, drone charging pads, cooling system, and a desktop computer.

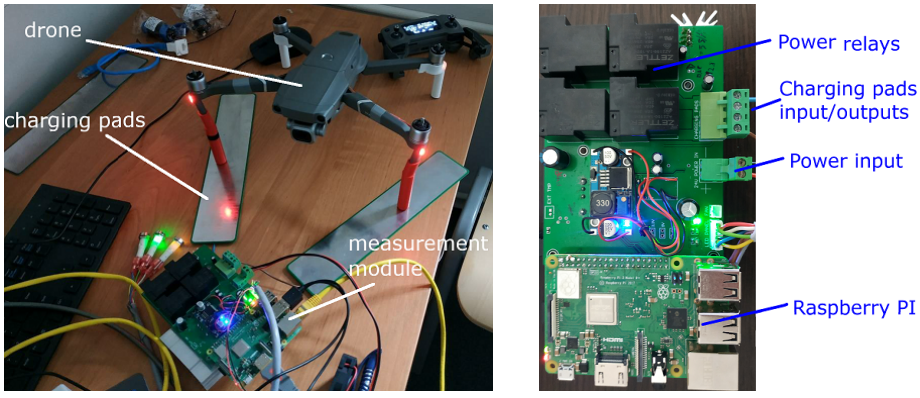

(a) DJI Mavic 2 Pro during experiments (b) measurement module

Fig. 4. Experimental setup

The measurement module was based on Raspberry Pi 3. The instrumentation was used to observe several system parameters (e.g., battery temperature, voltage, current) in real-time. All data were logged on the memory card. During measurements, the drone was powered, but all four electric motors were switched off, and the battery discharge rate was observed. The initial state of charge was 97%, and the final state of charge was 15%. The discharge time was 150 minutes. Knowing the amount of consumed energy and the abovementioned time, it was calculated that the onboard systems and sensors consume approximately $E_{\text{sub}} = 17.15$ J/s.

2.9. Battery model

It was necessary to include battery dynamics in the model to predict the actual battery state of charge and voltage. It was assumed that the battery was a new one and free from manufacturing errors. The aging effects were omitted in the model. The influence of temperature on the battery capacity was neglected [53].

The battery state of charge (SOC) was defined as [5, 54]:

$$\mathrm{SOC} = \mathrm{SOC}_0 - \int_0^t \frac{I(t)}{Q_{\mathrm{batt}}}\,\mathrm{d}t, \tag{39}$$

where: I – electric current, SOC_0 – initial battery state of charge, Q_{batt} – battery capacity. For a fully charged battery, the SOC = 100%, and for discharged 0%.

Next, to calculate SOC the electric current $I(t)$ must be calculated. The torque that is generated by the j-th BLDC motor is proportional to the electric current that flows through the motor:

$$\tau_j(t) = K_T I_j(t), \tag{40}$$

where coefficient K_T is the torque constant. Using (40) the current might be estimated as:

$$I_j(t) = \frac{\tau_j(t)}{K_T} \tag{41}$$

and $\tau_j(t)$ might be obtained from equation (34).

To calculate the voltage during the battery discharge process, the Shepherd model was used [55, 56]. This model is widely used to describe battery dynamics [57, 58]. It requires only several parameters, which can be obtained from the battery discharge curve [59, 60]. The battery voltage is modeled using the equation:

$$U_{\mathrm{disch}} = E_0 - K\frac{Q}{Q - \int_0^t I\,\mathrm{d}t}(I^* + I) + Ae^{-B\int_0^t I\,\mathrm{d}t} - RI \tag{42}$$

where: U_{disch} – actual battery voltage, E_0 – open circuit voltage of the battery, K – polarization resistance coeffcient, Q – battery capacity, t – time, I^* – low-frequency current dynamics, I – current, A – amplitude of the exponential zone, B – time constant inverse in the exponential zone, R – internal battery resistance (it was assumed to be 0.038442 Ω). The constants K = 0.0288 V/Ah, A = 1.2428 V and B = 15.6802 $(\mathrm{Ah})^{-1}$ were obtained according to [61].

2.10. Autopilot model

Quadrotors are nonlinear, multi-input/multi-output, and unstable systems. They are also underactuated objects, which means that the number of actuators (four independent electric motors) is smaller than the number of degrees of freedom (three

translations and three rotations) [62, 63]. As a result, the translational motions are coupled with angular rotations. The internal structure of the test platform autopilot was not known precisely (data and controller settings are not published by the Manufacturer). It was assumed that the drone uses cascaded proportional-integral-derivative (PID) controllers (Fig. 5) in each of the four control channels (altitude and three Euler angles) [64, 65].

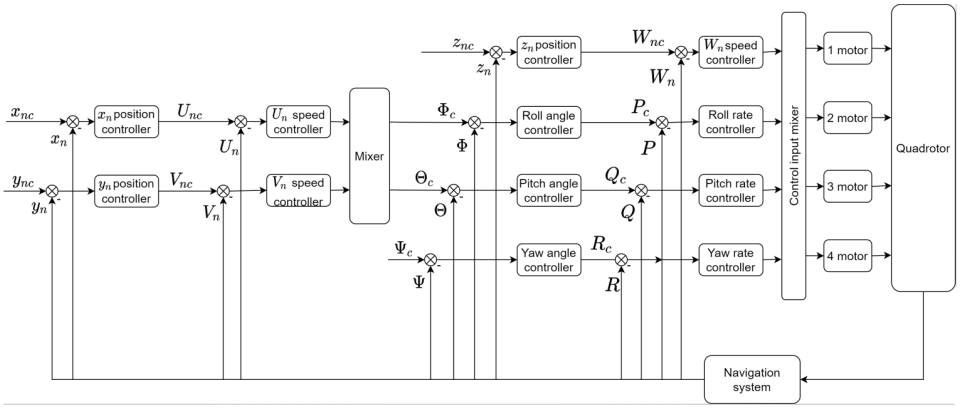

Fig. 5. Autopilot structure

Outputs from each autopilot channel were mixed to calculate the total angular speed for each propeller:

$$\begin{bmatrix} \Omega_{1c} \\ \Omega_{2c} \\ \Omega_{3c} \\ \Omega_{4c} \end{bmatrix} = \begin{bmatrix} 1 & 1 & 1 & 1 \\ 1 & 1 & -1 & -1 \\ 1 & -1 & -1 & 1 \\ 1 & -1 & 1 & -1 \end{bmatrix} \begin{bmatrix} U_1 \\ U_2 \\ U_3 \\ U_4 \end{bmatrix}, \tag{43}$$

where: U_1 is the control signal (angular rate of the motor) from the altitude autopilot, U_2 is the commanded signal from the roll autopilot, U_3 is the signal from the pitch autopilot and U_4 is the commanded value from the yaw autopilot. The altitude change is realized by changing the speed of all four propellers by the same value. The differences between propellers' angular rates result in thrust variations and quadcopter attitude changes. The anti-windup clamping method was used to prevent the PID controllers from integral term saturation. The drone performance was limited programmatically in the autopilot model settings according to the operator manual [35, 66] to the following values (P-mode): roll angle ±25°, pitch angle ±25°, ascent speed 3.5 m/s, and descent speed 4 m/s. The horizontal speed was saturated to 14 m/s. Maximum angular velocities (roll, pitch, and yaw) did not exceed 200°/s.

The waypoint follower block from MATLAB UAV Toolbox was used to generate x_{nc}, y_{nc}, z_{nc} coordinates of the lookahead point and the desired yaw angle Ψ_c (at each simulation step). A detailed description of the control system structure can be found in [67].

3. Results

3.1. Model validation (single trajectory)

The developed model was implemented into MATLAB/Simulink 2020b. The equations of motion were integrated using a fixed step fourth-order Runge-Kutta solver with step size 0.001 s. The simulations took place on the laptop computer with Processor Intel i7-8750H CPU @ 2.20 GHz and 16 GB RAM.

A set of 14 flight tests were performed on 20/21 May 2021 in Przasnysz airfield (Latitude 53.0050011, Longitude 20.9383297) in Poland to validate the developed model. The flight tests were realized mainly in the P-mode of the autopilot (thus limiting the drone's maneuverability) and partially using manual control. The trajectory was defined by a set of waypoints. The turn radius was set to 12 m. The flight data parameters were registered using only the embedded functionality without additional data logging equipment, since adding some onboard measurement devices could increase the mass of the drone and significantly reduce the performance. The experimental data sampling frequency was set to 10 Hz. Linear accelerations and angular rates were not recorded during the flight trials, which complicated the validation process. The resulting data logs were analyzed offline using Airdata online service [49] and then imported into MATLAB to compare with the simulation results. The initial conditions for the simulation (linear velocities, angular rates, position, and orientation) were set the same as those derived from the flight logs. Validation took place after completing the test campaign.

One of the flight tests (case number May-20th-2021-12-06PM-Flight-Airdata) was presented here as an example to illustrate the validation results and the achieved model reliability. The mean wind speed in the analyzed case was 6.5 m/s, and the mean wind azimuth was 301° (these values were measured on the airfield using an anemometer and estimated later from the obtained flight logs).

In Fig. 6, the comparison of Euler angles, position coordinates, and linear velocities with respect to the ground obtained from the flight test and numerical simulation is shown. The drone moved along the edges of a rectangular trajectory (Fig. 6a, flight direction was marked with black arrows).

The log duration (the time in the air and on the ground) was 1472 s. Roll (Fig. 6b) and pitch (Fig. 6c) angles were oscillatory due to the air turbulence. Yaw angle (Fig. 6d) decreased up to –1249°. It means that the object realized left turns (looking from aft) several times.

Both horizontal position coordinates (Fig. 6e, 6f) measured in the test agree well with the model predictions. The total mileage was 8199 m. At the beginning of

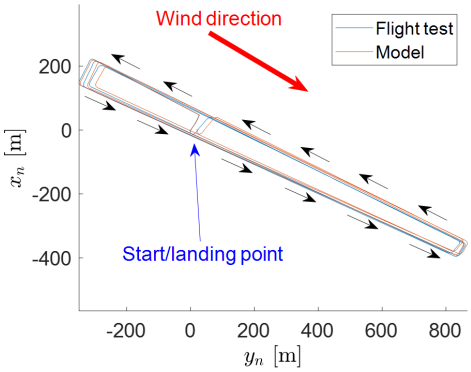

(a) quadrotor trajectory

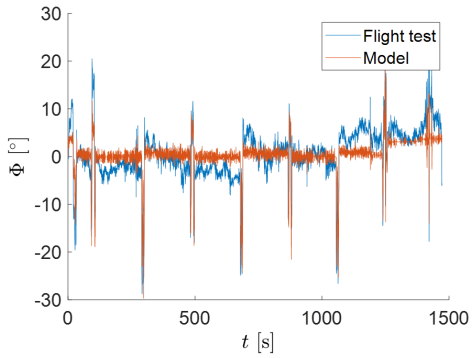

(b) roll angle

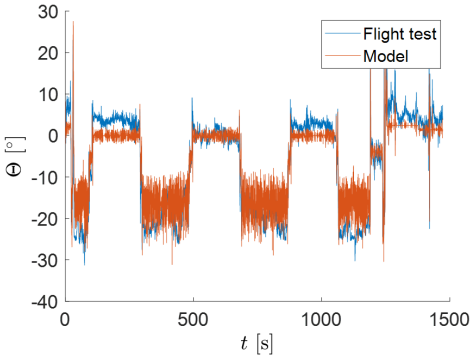

(c) pitch angle

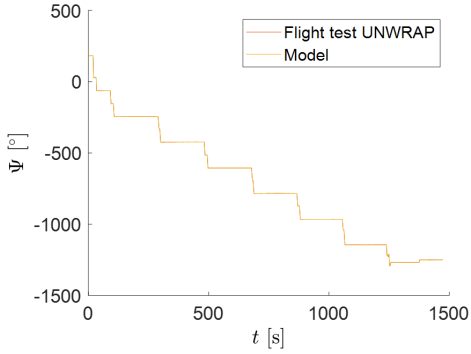

(d) yaw angle

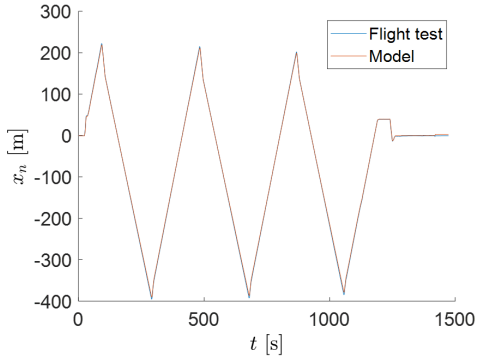

(e) horizontal position (North-South)

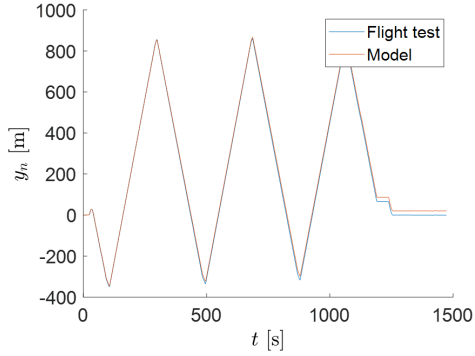

(f) horizontal position (East-West)

Fig. 6. Euler angles, position, and velocity comparison (flight test vs simulation)

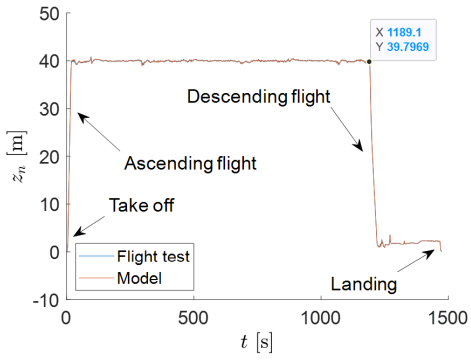

(g) vertical position

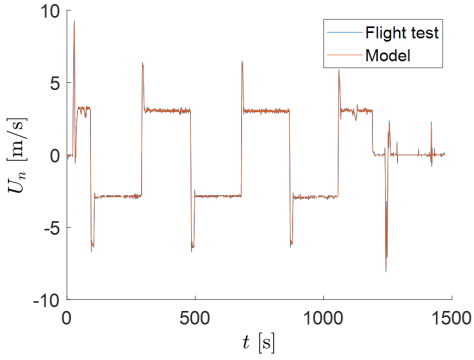

(h) horizontal velocity (North-South)

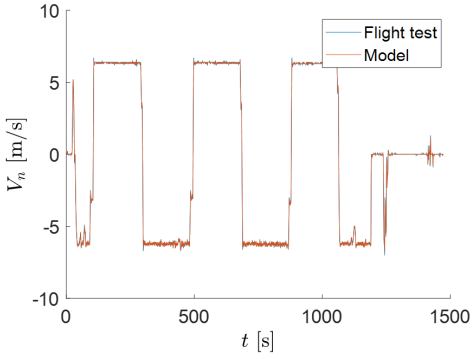

(i) horizontal velocity (East-West)

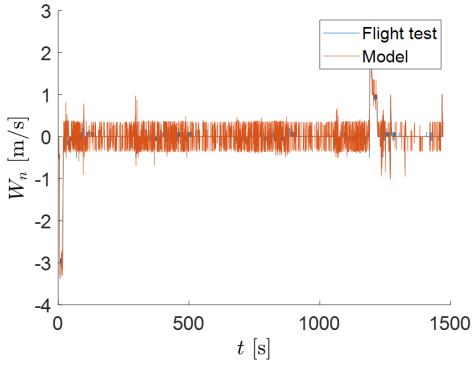

(j) vertical speed

Fig. 6. Euler angles, position, and velocity comparison (flight test vs simulation)

the flight, the altitude (Fig. 6g) increased from 0 m to 40 m. Then, the drone realized most of the mission at attitude 40 m. When the battery SOC was 15%, the drone velocity was limited to 12 m/s. In 1189 s, when the battery SOC dropped to 11%, the quadrotor entered the automatic landing mode. As a result, the altitude decreased rapidly to 2 m and was held constant nearly to the end of the flight. The further flight required manual control. Finally, the drone landed, and the attitude dropped to 0 m. The experimental results matched the simulation predictions accurately.

The two horizontal velocity components (Fig. 6h, 6i) form a rectangular signal. The vertical speed (Fig. 6j) at the beginning of the flight was –3 m/s because the drone was in ascending flight. Next, it oscillated about 0 m/s because the flight took place at a constant altitude. In 1200 s a 3 m/s peak was observed due to drone descent.

In Fig. 7, the propeller speed time history obtained from the simulation is presented. The propellers' angular rates were not measured during the flight, so it was impossible to compare them with the model directly.

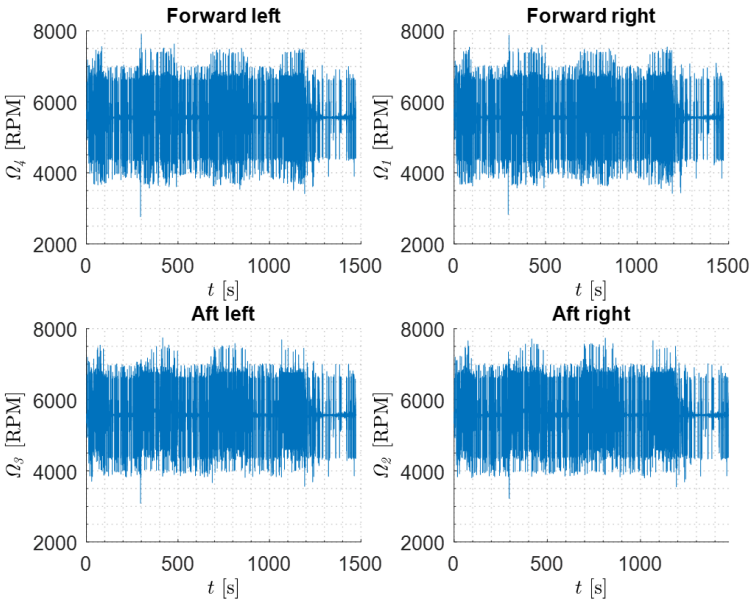

Fig. 7. Propellers angular speed obtained from simulation

With the aid of the simulation, it was predicted that the propeller minimum speed achieved during the analyzed test would be approximately 4000 RPM and a maximum of 7700 RPM.

In Fig. 8a, the comparison of the amount of energy consumed by the quadrotor is shown. In Fig. 8b, the battery state of charge comparison between the flight trials and simulation is presented. In Fig. 8c, the battery voltage is presented (total and for individual battery cells).

During the mission, all the onboard available energy was spent (Fig. 8a). The experimental results (in the legend "Flight data – E_c") match well the numerical predictions of total energy consumption ("Model – E_c"). From the simulation results it might be concluded that the total energy consumed by the motors ("Model – E_m") was 49.8243 Wh. The energy consumed by the subsystems ("Model – E_s") was approximately 6.50119 Wh (13% of the energy spent on propulsion and 11.54% of the total energy), which means that this component plays a significant role in the total energy balance.

The state of charge (Fig. 8b) during the experiments was recorded with a sensor resolution of 1%. The initial state of charge was 95%. The curve decreased linearly. At 59 s, the SOC was 90%. At the end of the real flight, SOC was 1%. It might be expected that this value should be 0%, but the mentioned quantity is never displayed in the flight logs. SOC equal 0% was defined by the producer as a situation when the total battery voltage drops to 14.2 V. It means that the battery has a small amount of reserve power that could be used to continue the flight for approximately 2 minutes after reaching 0% SOC. In this way, the drone is still able

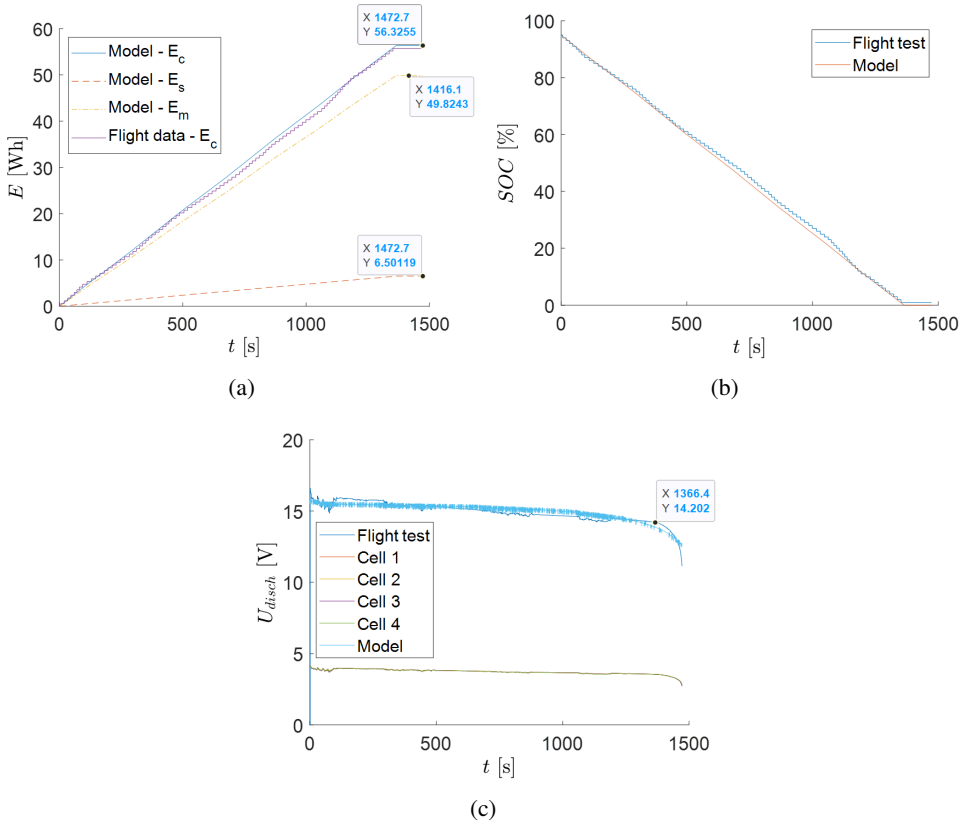

Fig. 8. Battery model validation (experiment vs simulation)

to land safely. After 1364 s, the lines in Figs. 8a, and 8b were flat, but the drone was still operating. The test results agreed with the model predictions accurately.

The total voltage (Fig. 8c) is a sum of voltages from individual cells. A typical discharge curve for a lithium-polymer battery was obtained. The voltage of a fully charged device is higher than the discharged one. At the beginning of the flight, the total voltage was 16.6 V and decreased slowly with time. At the end of the mission, the total voltage rapidly dropped to 11.134 V. The curves of voltage for each cell coincided with each other.

3.2. Model validation (multiple trajectories)

The simulation should correctly predict flight parameters and consumed energy for arbitrary quadrotor trajectories. The comparison between reality and simulation was evaluated for each flight trial to check this issue. To measure the model reliability, the Root Mean Squared Errors (RMSE) were calculated. For the sake of manuscript length, only results for several flight trials were presented (Table 1).

Table 1. Degree of similarity between reality and the simulation

Flight test date	May-20th-2021-12-06PM	May-20th-2021-03-09PM	May-20th-2021-04-54PM	May-20th-2021-05-31PM	May-20th-2021-06-34PM	May-20th-2021-12-37PM
Parameter	RMSE					
Φ [°]	3.421828	0.803162	0.961475	1.092269	1.473645	0.916345
Θ [○]	4.739559	4.148219	2.968515	7.051444	4.696304	6.082776
Ψ [°]	0.808468	2.563347	2.866789	3.709629	3.068936	2.593994
x_n [m]	2.619691	3.434738	2.622405	11.176327	5.681687	2.799612
y_n [m]	13.609700	9.312233	14.669029	63.788978	18.711312	3.272188
z_n [m]	0.064751	0.064690	0.065718	0.087423	0.062609	0.074872
U_n [m/s]	0.169765	0.176271	0.205990	0.481001	0.476275	0.175708
V_n [m/s]	0.166286	0.191627	0.196962	1.197636	0.654725	0.169507
W_n [m/s]	0.148954	0.149815	0.144161	0.190237	0.170198	0.159187

The smallest values of RMSE were obtained for the drone's vertical position z_n. Some discrepancies were observed for pitch angle Θ. The differences also result from varying wind conditions.

The comparison between energy consumed in reality and predicted by the simulation is presented in Table 2.

Table 2. Energy consumed by the drone

Flight test date	May-20th-2021-12-06PM	May-20th-2021-03-09PM	May-20th-2021-04-54PM	May-20th-2021-05-31PM	May-20th-2021-06-34PM	May-20th-2021-12-37PM
Initial SOC [%]	95	99	99	98	100	100
Energy [Wh] (experiment)	55.7326	58.3145	58.2042	57.5113	58.6971	32.0166
Energy [Wh] (model)	56.3255	58.1258	58.2721	57.5016	58.8154	31.2339
Flight time [s]	1472.7	1542.4	1615.1	1234.5	1229.4	730.9

In the last case, the flight time was the shortest, so the amount of consumed energy was also the smallest. The obtained results indicate that the experimental results match the model predictions accurately.

3.3. Monte-Carlo simulation

Next, the Monte-Carlo simulation was evaluated to investigate further the model reliability. The uncertainties in quadrotor mass properties, initial conditions, and wind parameters were considered [68]. The disturbances were modeled

individually as a Gaussian [69]. Each parameter was calculated as a sum of two numbers: the nominal value and the uncertainty with mean value μ and standard deviation σ. The uncertainties used in the simulation are presented in Table 3.

Table 3. Parameters for the Monte-Carlo simulation

No.	Parameter	Mean value μ	Standard deviation σ	Unit
1	m	0.960	0.020	kg
2	I_{xx}	$4.25582 \cdot 10^{-3}$	0.0005	kg·m^2
3	I_{yy}	$4.724053 \cdot 10^{-3}$	0.0005	kg·m^2
4	I_{zz}	$7.859282 \cdot 10^{-3}$	0.0005	kg·m^2
5	U_0	0	0.5	m/s
6	V_0	0	0.1	m/s
7	W_0	0	0.1	m/s
8	P_0	0	3	°/s
9	Q_0	0	3	°/s
10	R_0	0	3	°/s
11	Φ_0	0	1	°
12	Θ_0	8.2	1	°
13	Ψ_0	182.1	1	°
15	x_{n0}	0	0.2	m
16	y_{n0}	0	0.2	m
17	z_{n0}	0	0.2	m
18	$V_{W\,\mathrm{tot}}$	6.5	0.5	m/s
19	Ψ_W	301	10	°

The Marsenne-Twister algorithm was used to pseudorandomly generate the abovementioned parameters. The random seed was set to 0 before numerical calculations. For each scenario, the number of simulation runs was equal to 100 (it means that 600 runs were evaluated). Simulink "Accelerator" mode was used to increase model execution speed and reduce the simulation time. The autopilot settings were the same for each simulation run.

In Fig. 9, the kernel density estimators of the total consumed energy are presented for several flight trials (datatips were added for clarity of the results). The black vertical line means the amount of energy consumed in a real flight test.

The modeling uncertainties have affected the amount of consumed energy. For each case, the real value of consumed energy is very close to the maximum of the curve obtained from numerical simulation.

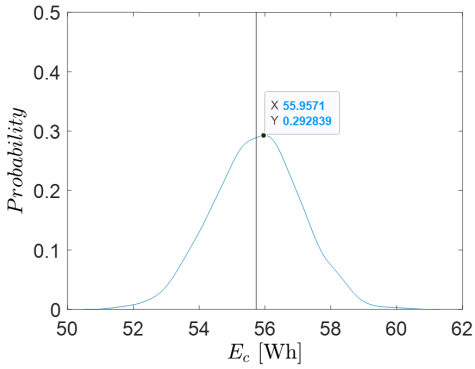

(a) May-20th-2021-12-06PM

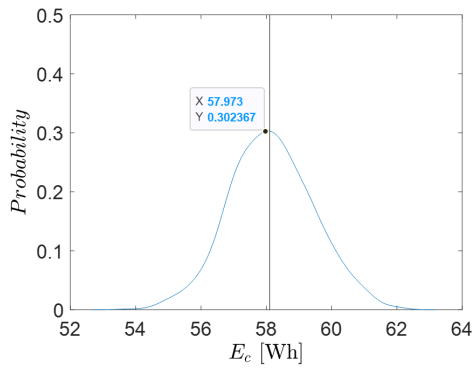

(b) May-20th-2021-03-09PM

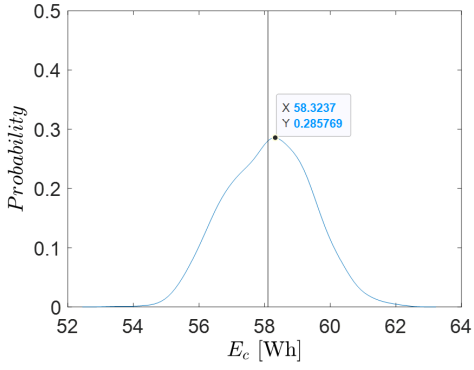

(c) May-20th-2021-04-54PM

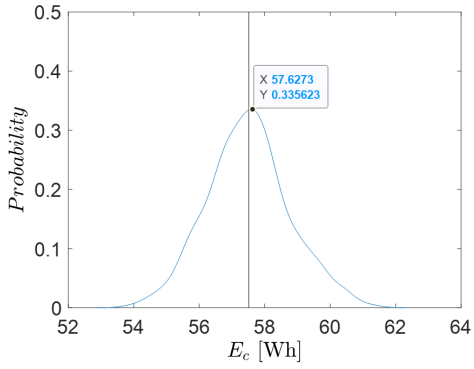

(d) May-20th-2021-05-31PM

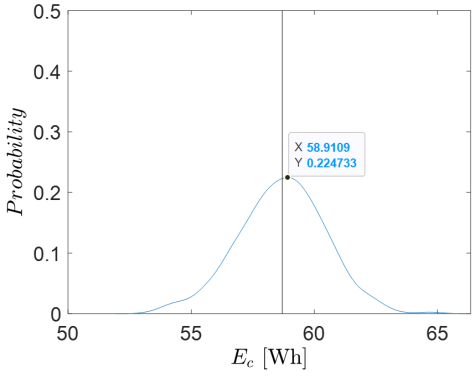

(e) May-20th-2021-06-34PM

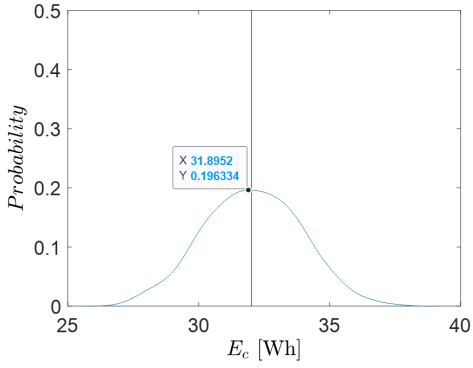

(f) May-20th-2021-12-37PM

Fig. 9. Consumed energy

4. Conclusions

In this paper, the nonlinear mathematical model of the quadrotor was developed and validated. The modified DJI MAVIC 2 Pro drone was used as a test platform. The model parameters were obtained during stationary tests in laboratory conditions. Next, the flight tests took place in windy conditions. The wind effect was one of the main difficulties in predicting the object's behavior accurately. The experimental data correlates with the results of the numerical simulation. The obtained model has a practical value because it could be used to predict the drone flight parameters and energy consumption during the mission.

The main advantage of the model is the possibility of detailed insight into system dynamics. When compared to black-box models, the presented approach requires a set of physical parameters, but on the other hand, those numbers might be obtained quite easily from manufacturer datasheets, using CAD models, and experimental testing. In that way, the presented model might be adopted for other quadrotors. In comparison with aeromechanics models, the proposed simulation is computationally effective because there is no need to calculate the induced velocity.

Several contributions of this work might be mentioned. First, the presented study extends the works of Yacef et al. [5, 7, 8] and Jaafar [50] as the energy consumed by the onboard electronic subsystems is included in the model. The energy consumed by the propellers was several times higher when compared to the energy spent on the operation of other onboard subsystems. On the other hand, neglecting this energy might lead to an overestimation of flight endurance.

Second, the battery dynamics is also incorporated into the simulation, which makes it more realistic. The battery voltage and state of charge might be predicted accurately.

Third, it was discussed how to obtain model parameters. The significant disadvantage of the proposed model is the number of parameters that must be known. However, most of them could be found quite easily in laboratory conditions or can be obtained from the producer manual.

Fourth, in this paper, the analysis for the whole mission is considered. Several flight trials were performed to prove the model's reliability. This fact partially fills the literature gap. In the literature, validation is often presented for a small portion of the time. Sometimes, even pure datasets (without relating to any model) are shown [4].

Fifth, a Monte-Carlo simulation was realized to evaluate the model's reliability. Uncertainties in model parameters influence the prediction of consumed energy, but the results are close enough to the measured values. The obtained results also extend the research presented in [70].

Future works might concentrate on flight tests to gather more data in order to create a detailed dataset and increase the reliability of the model. The propulsion model could be improved to include various aerodynamic phenomena. Wind tunnel tests of the isolated fuselage of the drone might be evaluated to improve the

aerodynamic coefficients database. Additional lightweight onboard instrumentation might be considered to increase the availability of the flight parameters registered during the flight. Also, precise wind measurements might be conducted during the flight tests to understand the drone's motion in various atmospheric conditions.

Acknowledgments

This work is supported by National Center for Research and Development (NCBiR) [grant number 4/1.1.1/2020 "Renewable Energy Sources (RES) in transport"].

Special thanks to Marcin Kasprzyk for conducting the flight trials.

Flight data from 14 flight tests and model parameters are available in "csv" and "mat" formats at request at the e-mail address of the corresponding author.

References

[1] Z. He and L. Zhao. A simple attitude control of quadrotor helicopter based on Ziegler-Nichols rules for tuning PD parameters. *The Scientific World Journal*, 2014: 280180, 2014. doi: 10.1155/2014/280180.

[2] P. Jimenez, P. Lichota, D. Agudelo, and K. Rogowski. Experimental validation of total energy control system for UAVs. *Energies*, 13(1):14, 2020. doi: 10.3390/en13010014.

[3] C. Aoun, N. Daher, and E. Shammas. An energy optimal path-planning scheme for quadcopters in forests. *2019 IEEE 58th Conference on Decision and Control (CDC)*, pages 8323–8328, Nice, France, 11–13 December 2019. doi: 10.1109/CDC40024.2019.9029345.

[4] T.A. Rodrigues, J. Patrikar, A. Choudhry, J. Feldgoise, V. Arcot, A. Gahlaut, S. Lau, B. Moon, B. Wagner, H.S. Matthews, S. Scherer, and C. Samaras. In-flight positional and energy use data set of a DJI Matrice 100 quadcopter for small package delivery. *Scientific Data*, 8:155, 2021. doi: 10.1038/s41597-021-00930-x.

[5] F. Yacef, N. Rizoug, and L. Degaa. Energy-efficiency path planning for quadrotor UAV under wind conditions. *2020 7th International Conference on Control, Decision and Information Technologies (CoDIT)*, pages 1133–1138, Prague, Czech Republic, 29 June–2 July 2020. doi: 10.1109/CoDIT49905.2020.9263968.

[6] F. Yacef, O. Bouhali, M. Hamerlain, and N. Rizoug. Observer-based adaptive fuzzy backstepping tracking control of quadrotor unmanned aerial vehicle powered by Li-ion battery. *Journal of Intelligent and Robotic Systems*, 84(1–4):179–197, 2016. doi: 10.1007/s10846-016-0345-0.

[7] F. Yacef, N. Rizoug, O. Bouhali, and M. Hamerlain. Optimization of energy consumption for quadrotor UAV. *International Micro Air Vehicle Conference and Flight Competition (IMAV) 2017*, Toulouse, France, 18-21 September 2017.

[8] F. Yacef, N. Rizoug, L. Degaa, O. Bouhali, and M. Hamerlain. Trajectory optimisation for a quadrotor helicopter considering energy consumption. *2017 4th International Conference on Control, Decision and Information Technologies (CoDIT)*, pages 1030–1035, Barcelona, Spain, 5–7 April 2017. doi: 10.1109/CoDIT.2017.8102734.

[9] G. Jia, S. Gong, R. Guo, and M. Li. Energy consumption model of BLDC quadrotor UAVs for mobile communication trajectory planning. *TechRxiv*. doi: 10.36227/techrxiv.19181228.v1.

[10] F. Morbidi, R. Cano, and D. Lara. Minimum-energy path generation for a quadrotor UAV. *2016 Ieee International Conference on Robotics and Automation (ICRA)*, pages 1492–1498, Stockholm, Sweden, 16–21 May 2016. doi: 10.1109/ICRA.2016.7487285.

[11] S. Jee and H. Cho. Comparing energy consumption following flight pattern for quadrotor. *Journal of IKEEE*, 22(3):747–753, 2018. doi: 10.7471/ikeee.2018.22.3.747.

[12] C.W. Chan and T.Y. Kam. A procedure for power consumption estimation of multi-rotor unmanned aerial vehicle. *Journal of Physics: Conference Series*, 1509:012015, 2020. doi: 10.1088/1742-6596/1509/1/012015.

[13] Y. Wang, Y. Wang, and B. Ren. Energy saving quadrotor control for field inspection. *IEEE Transactions on Systems, Man, and Cybernetics: Systems*, 52(3):1768–1777, 2020. doi: 10.1109/TSMC.2020.3037071.

[14] H. Lu, K. Chen, X.B. Zhai, B. Chen, and Y. Zhao. Tradeoff between duration and energy optimization for speed control of quadrotor unmanned aerial vehicle. *2018 IEEE Symposium on Product Compliance Engineering – Asia (ISPCE-CN)*, pages 1–5, Shenzhen, China, 5–7 December 2018. doi: 10.1109/ISPCE-CN.2018.8805801.

[15] N. Bezzo, K. Mohta, C. Nowzari, I. Lee, V. Kumar, and G. Pappas. Online planning for energy-efficient and disturbance-aware UAV operations. *2016 IEEE/RSJ International Conference on Intelligent Robots and Systems (IROS)*, pages 5027–5033, Daejeon, Korea, 9–14 October 2016. doi: 10.1109/IROS.2016.7759738.

[16] V. Agarwal and R.R. Tewari. Improving energy efficiency in UAV attitude control using deep reinforcement learning. *Journal of Scientific Research*, 65(3):209–219, 2021.

[17] A. Korneyev, M. Gorobetz, I. Alps, and L. Ribickis. Adaptive traction drive control algorithm for electrical energy consumption minimisation of autonomous unmanned aerial vehicle. *Electrical, Control and Communication Engineering*, 15(2):62–70, 2019. doi: 10.2478/ecce-2019-0009.

[18] J.F. Roberts, J.-C. Zufferey, and D. Floreano. Energy management for indoor hovering robots. *2008 IEEE/RSJ International Conference on Intelligent Robots and Systems*, pages 1242–1247, Nice, France, 22–26 September 2008. doi: 10.1109/IROS.2008.4650856.

[19] A.S. Prasetia, R.-J. Wai, Y.-L. Wen, and Y.-K. Wang. Mission-based energy consumption prediction of multirotor UAV. *IEEE Access*, 7:33055–33063, 2019. doi: 10.1109/ACCESS.2019.2903644.

[20] X. Wu, J. Zeng, A. Tagliabue, and M. W. Mueller. Model-free online motion adaptation for energy-efficient flight of multicopters. *Arxiv*. doi: 10.48550/arXiv.2108.03807.

[21] C. Di Franco and G. Buttazzo. Energy-aware coverage path planning of UAVs. *2015 IEEE International Conference on Autonomous Robot Systems and Competitions*, pages 111–117, Vila Real, Portugal, 08–10 April 2015. doi: 10.1109/ICARSC.2015.17.

[22] T. Dietrich, S. Krug, and A. Zimmermann. An empirical study on generic multicopter energy consumption profiles. *2017 Annual IEEE International Systems Conference (SysCon)*, pages 1–6, Montreal, QC, Canada, 24–27 April 2017. doi: 10.1109/SYSCON.2017.7934762.

[23] H.V. Abeywickrama, B.A. Jayawickrama, Y. He, and E. Dutkiewicz. Empirical power consumption model for UAVs. *2018 IEEE 88th Vehicular Technology Conference (VTC-Fall)*, pages 1-5, Chicago, IL, USA, 27–30 August 2018. doi: 10.1109/VTCFall.2018.8690666.

[24] R. Shivgan and Z. Dong. Energy-efficient drone coverage path planning using genetic algorithm. *2020 IEEE 21st International Conference on High Performance Switching and Routing (HPSR)*, pages 1–6, Newark, NJ, USA, 11–14 May 2020. doi: 10.1109/HPSR48589.2020.9098989.

[25] C. Di Franco and G. Buttazzo. Coverage path planning for UAVs photogrammetry with energy and resolution constraints. *Journal of Intelligent & Robotic Systems*, 83:445–462, 2016. doi: 10.1007/s10846-016-0348-x.

[26] N. Gao, Y. Zeng, J. Wang, D. Wu, C. Zhang, Q. Song, J. Qian and S. Jin. Energy model for UAV communications: Experimental validation and model generalization. *China Communications*, 18(7):253–264, 2021. doi: 10.23919/JCC.2021.07.020.

[27] N. Kreciglowa, K. Karydis, and V. Kumar, Energy efficiency of trajectory generation methods for stop-and-go aerial robot navigation. *2017 International Conference on Unmanned Aircraft Systems (ICUAS)*, pages 656–662, Miami, USA, 13–16 June 2017. doi: 10.1109/ICUAS.2017.7991496.

[28] P. Pradeep, S.G. Park, and P. Wei. Trajectory optimization of multirotor agricultural. *2018 IEEE Aerospace Conference*, pages 1–7, Big Sky, USA, 3–10 March 2018. doi: 10.1109/AERO.2018.8396617.

[29] M-h. Hwang, H-R. Cha and S.Y. Jung. Practical endurance estimation for minimizing energy consumption of multirotor unmanned aerial vehicles. *Energies*, 11(9):2221, 2018. doi: 10.3390/en11092221.

[30] A. Abdilla, A. Richards, and S. Burrow. Power and endurance modelling of battery-powered rotorcraft. *2015 IEEE/RSJ International Conference on Intelligent Robots and Systems (IROS)*, pages 675–680, Hamburg, Germany, 28 September–2 October 2015. doi: 10.1109/IROS.2015.7353445.

[31] J. Apeland, D. Pavlou, and T. Hemmingsen. Suitability Analysis of implementing a fuel cell on a multirotor drone. *Journal of Aerospace Technology and Management*, 12:e3220, 2020. doi: 10.5028/jatm.v12.1172.

[32] Z. Liu, R. Sengupta and A. Kurzhanskiy. A power consumption model for multi-rotor small unmanned aircraft systems. *2017 International Conference on Unmanned Aircraft Systems (ICUAS)*, pages 310–315, Miami, FL, USA, 13–16 June 2017. doi: 10.1109/ICUAS.2017.7991310.

[33] L. Zhang, A. Celik, S. Dang, and B. Shihada. Energy-efficient trajectory optimization for UAV-assisted IoT networks. *IEEE Transactions on Mobile Computing*, 21(12):4323–4337, 2022. doi: 10.1109/TMC.2021.3075083.

[34] Y. Chen, D. Baek, A. Bocca, A. Macii, E. Macii, and M. Poncino. A case for a battery-aware model of drone energy consumption. *2018 IEEE International Telecommunications Energy Conference (INTELEC)*, pages 1–8, Turino, Italy, 7–11 October 2018. doi: 10.1109/INTLEC.2018.8612333.

[35] [Online]. https://www.dji.com/pl/mavic-2/info, [Accessed on: 13 July 2021].

[36] National Aeronautics and Space Administration, U.S. Standard Atmosphere, 1976, Washington, D.C., 1976.

[37] P.H. Zipfel. *Modeling and Simulation of Aerospace Vehicle Dynamics*. American Institute of Aeronautics and Astronautics. Reston, USA, 2000.

[38] D. Allerton. *Principles of Flight Simulation*. John Wiley and Sons, 2009.

[39] B.L. Stevens, F.L. Lewis, and E.N. Johnson. *Aircraft Control and Simulation. Dynamics, Controls Design, and Autonomous Systems*. John Wiley and Sons, 2015.

[40] M. Dreier. *Introduction to Helicopter and Tiltrotor Simulation*. American Institute of Aeronautics and Astronautics. Reston, USA, 2007.

[41] P. Lichota, F. Dul, and A. Karbowski. System identification and LQR controller design with incomplete state observation for aircraft trajectory tracking. *Energies*, 13(20):5354, 2020. doi: 10.3390/en13205354.

[42] M. Abzug. *Computational Flight Dynamics*. American Institute of Aeronautics and Astronautics. Reston, USA, 1998.

[43] S.K. Phang, C. Cai, B.M. Chen, and T.H. Lee. Design and Mathematical Modeling of a 4-Standard-Propeller (4SP) Quadrotor. In: *Proceedings of the 10th World Congress on Intelligent Control and Automation*, pages 3270–3275, Beijing, China, 6–8 July 2012. doi: 10.1109/WCICA.2012.6358437.

[44] J. Sanketi, R. Kasliwal, S. Raghavan, and S. Awan. Modelling and simulation of a multi-quadcopter concept. *International Journal of Engineering Research & Technology (IJERT)*, 5(10):566–571, 2016.

[45] N.M. Salma and K. Osman. Modelling and PID control system integration for quadcopter DJIF450 attitude stabilization. *Indonesian Journal of Electrical Engineering and Computer Science*, 19(3):1235–1244. doi: 10.11591/ijeecs.v19.i3.pp1235-1244.

[46] P. Pounds, R. Mahony, and P. Corke. Modelling and control of a large quadrotor robot. *Control Engineering Practice*, 18(7):691–699, 2010. doi: 10.1016/j.conengprac.2010.02.008.

[47] Z. Benić, P. Piljek, and D. Kotarski. Mathematical modelling of unmanned aerial vehicles with four rotors. *Interdisciplinary Description of Complex Systems*, 14(1):88–100, 2016. doi: 10.7906/indecs.14.1.9.

[48] I.M. Salameh, E.M. Ammar, and T.A. Tutunji. Identification of quadcopter hovering using experimental data. *2015 IEEE Jordan Conference on Applied Electrical Engineering and Computing Technologies (AEECT)*, pages 1–6, Amman, Jordan, 3–5 November 2015. doi: 10.1109/AEECT.2015.7360559.

[49] [Online]. Available: https://airdata.com [Accessed on: 27 January 2022].

[50] W. Jaafar and H. Yanikomeroglu. Dynamics of quadrotor UAVs for aerial networks: An energy perspective. *Arxiv*, 2019. doi: 10.48550/arXiv.1905.06703.

[51] P. Pradeep and P. Wei. Energy efficient arrival with rta constraint for multirotor eVTOL in urban air mobility. *Journal of Aerospace Information Systems*, 16(7):1–15, 2019. doi: 10.2514/1.I010710.

[52] F. Morbidi and D. Pisarski. Practical and accurate generation of energy-optimal trajectories for a planar quadrotor. *2021 IEEE International Conference on Robotics and Automation (ICRA)*, pages 355–361, Xi'an, China, 30 May–5 June 2021. doi: 10.1109/ICRA48506.2021.9561395.

[53] T. Mesbahi, N. Rizoug, P. Bartholomeus, and P. Le Moigne. Li-ion battery emulator for electric vehicle applications. *2013 IEEE Vehicle Power and Propulsion Conference (VPPC)*, pages 1–8, Beijing, China, 15–18 October 2013. doi: 10.1109/VPPC.2013.6671688.

[54] F. Li, W.-P. Song, B.-F. Song, and H. Zhang, Dynamic modeling, simulation, and parameter study of electric quadrotor system of Quad-Plane UAV in wind disturbance environment. *International Journal of Micro Air Vehicles*, 13:1–23, 2021. doi: 10.1177/17568293211022211.

[55] O. Tremblay and L-A. Dessaint. Experimental validation of a battery dynamic model for ev applications. *World Electric Vehicle Journal*, 3(2):289–298, 2009. doi: 10.3390/wevj3020289.

[56] S.M. Mousavi and M. Nikdel. Various battery models for various simulation studies and applications. *Renewable and Sustainable Energy Reviews*, 32:477–485, 2014. doi: 10.1016/j.rser.2014.01.048.

[57] S.M. Azam. *Battery Identification, Prediction and Modelling*. Master Thesis, Colorado State University, Fort Collins, Colorado, USA, 2018.

[58] E. Raszmann, K. Baker, Y. Shi, and D. Christensen. Modeling stationary lithium-ion batteries for optimization and predictive control. *2017 IEEE Power and Energy Conference at Illinois (PECI)*, pages 1–7, Champaign, IL, USA, 23–24 February 2017. doi: 10.1109/PECI.2017.7935755.

[59] H. Hemi, N.K. M'Sirdi, and A. Naamane. A new proposed shepherd model of a li-ion open circuit battery based on data fitting. IMAACA 2019, Lisbon, Portugal, 2019.

[60] [Online]: https://www.mathworks.com/help/physmod/sps/powersys/ref/battery.html. [Accessed on: 9 October 2021].

[61] H. Hinz. Comparison of lithium-ion battery models for simulating storage systems in distributed power generation. *Inventions*, 4(3):41, 2019. doi: 10.3390/inventions4030041.

[62] L.E. Romero, D.F. Pozo, and J.A. Rosales. Quadcopter stabilization by using PID controllers. *Maskana*, 5:175–186, 2016.

[63] A. Rodić and G. Mester. The modeling and simulation of an autonomous quad-rotor microcopter in a virtual outdoor scenario. *Acta Polytechnica Hungarica*, 8(4):107–122, 2011.

[64] A.L. Salih, M. Moghavvemi, H.A.F. Mohamed, and K.S. Gaeid. Flight PID controller design for a UAV quadrotor. *Scientific Research and Essays*, 5(23):3660–3667, 2010.

[65] V. Brito, A. Brito, L.B. Palma, and P. Gil. Quadcopter control approaches and performance analysis. In *Proceedings of the 15th International Conference on Informatics in Control, Automation and–Robotics – Volume 1: ICINCO*, pages 86–93, Porto, Portugal, 29–31 July, 2018. doi: 10.5220/0006902600960103.

[66] [Online]. Available: https://www.dji.com/pl/downloads/products/mavic-2. [Accessed on: 7 August 2021].

[67] M. Jacewicz, M. Żugaj, R. Głębocki, and P. Bibik. Quadrotor model for energy consumption analysis. *Energies*, 15(19):7136, 2022. doi: 10.3390/en15197136.

[68] M. Jacewicz, P. Lichota, D. Miedziński, and R. Głębocki. Study of model uncertainties influence on the impact point dispersion for a gasodynamicaly controlled projectile. *Sensors*, 22(9):3257, 2022. doi: 10.3390/s22093257.

[69] M. Jacewicz, R. Głębocki, and R. Ożóg. Monte-Carlo based lateral thruster parameters optimization for 122 mm rocket. In: R. Szewczyk, C. Zieliński, M. Kaliczyńska (eds.) *Automation 2020: Towards Industry of the Future. AUTOMATION 2020. Advances in Intelligent Systems and Computing*, volume 1140, pages 125–134, Springer, 2020. doi: 10.1007/978-3-030-40971-5_12.

[70] C. Coulombe, J.-F. Gamache, A. Mohebbi, C. Abolfazl, U. Chouinard and S. Achiche. Applying robust design methodology to a quadrotor drone. In *Proceedings of the 21st International Conference on Engineering Design (ICED17)*, vol 4: Design Methods and Tools, Vancouver, Canada, 21–25 August 2017.